# Direct Probing of a Large Spin−Orbit Coupling in the FeSe Superconducting Monolayer on STO

Khalil Zakeri,* Dominik Rau, Jasmin Jandke, Fang Yang, Wulf Wulfhekel, and Christophe Berthod

ABSTRACT: Spin−orbit coupling (SOC) is a fundamental physical interaction, which describes how the electrons' spin couples to their orbital motion. It is the source of a vast variety of fascinating phenomena in nanostructures. Although in most theoretical descriptions of high-temperature superconductivity SOC has been neglected, including this interaction can, in principle, revise the microscopic picture. Here by preforming energy-, momentum-, and spin-resolved spectroscopy experiments we demonstrate that while probing the dynamic charge response of the FeSe monolayer on strontium titanate, a prototype two-dimensional high-temperature superconductor using electrons, the scattering cross-section is spin dependent. We unravel the origin of the observed phenomenon and show that SOC in this two-dimensional superconductor is strong. We anticipate that such a strong SOC can have several consequences on the electronic structures and may compete with other pairing scenarios and be crucial for the mechanism of superconductivity.

KEYWORDS: iron chalcogenides, FeSe monolayer, strontium titanate, high-temperature superconductivity, two-dimensional superconductors, spin−orbit coupling, spin-polarized high-resolution electron energy-loss spectroscopy
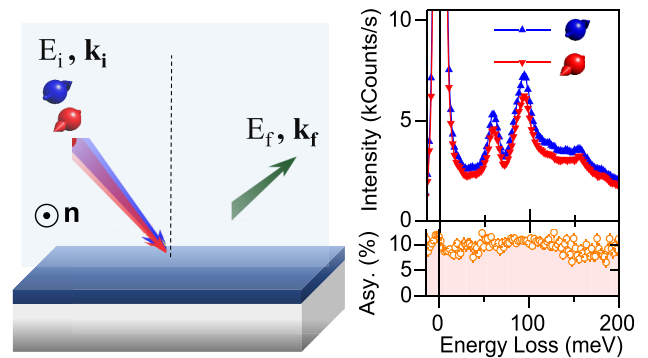
INTRODUCTION

The fundamental interaction describing the microscopic coupling mechanism between the spin and orbital degrees of freedom of electrons in solids is the so-called spin−orbit coupling (SOC).[1,2] This interaction, which is a relativistic effect, is an essential ingredient for describing many emergent phenomena observed in condensed-matter systems. For instance, a large SOC in combination with other symmetry aspects can lead to the appearance of topological phases in solids. Examples of this kind are the topological insulators, where a large SOC leads to the formation of the topologically protected surface states and spin momentum locking.[3−7] In order to figure out whether or not a material exhibits topological electronic states and to which topological classes these states belong, one requires to quantify the strength of SOC.

Although the phenomenon of high-temperature superconductivity is, by itself, a fascinating phenomenon, combined with topological aspects of matter it would lead to an even more exotic state of matter, e.g., topological superconductivity and the formation of the Majorana states.[8−10] These states, which obey non-Abelian statistics, can be used to realize topological quantum computers.[11] In most of the proposals for realizing these interesting concepts it is suggested to attach a low-dimensional superconductor to a topological material or semiconductor heterostructures with a large SOC.[9] However, under some circumstances if SOC in a low-dimensional superconductor is sufficiently large, one expects to observe topological states in a single material.[12] An ideal candidate for such an observation would be a single layer of FeSe grown on $SrTiO_3(001)$, an ideal two-dimensional high-temperature superconductor (HTSC).[13−19] In the case of ultrathin films the inversion symmetry in the direction perpendicular to the surface is broken. A large SOC together with the broken inversion symmetry can provide the necessary fundamental basis required for the observation of topological states in the

system.[20,21] Hence a direct probing of SOC in this class of materials is essential in connection with the possibility of the formation of topological states.

Irrespective of the importance of SOC for the topological superconductivity, the presence of this interaction is of prime importance to understand the underlying physics of HTSC in general.[20,22] Generally the impact of SOC becomes increasingly important when reducing the systems' dimensionality. This is due to the emergence of new symmetry aspects in low-dimensional solids. Surprisingly, so far no direct signature of SOC and its impact in ultrathin (two-dimensional) HTSCs have been reported experimentally.

Here by performing high-resolution spectroscopy of spin-polarized slow electrons on epitaxial FeSe monolayers grown on Nb-doped strontium titanate $SrTiO_3(001)$ (hereafter STO), a prototypical two-dimensional superconductor, we demonstrate that the frequency- and momentum-dependent scattering cross-section depends strongly on the spin of the incoming electron. A careful analysis of the spectra reveals that the observed effect is due to the presence of a considerably large SOC in this system. Such a large SOC together with other symmetry aspects provides the required ingredients for the formation of topologically protected states and would shed light on the mysterious origin of superconductivity in this system.

RESULTS

The epitaxial FeSe monolayer was grown by molecular beam epitaxy on STO(001). The dynamic charge response of the system was probed by means of spin-polarized high-resolution electron energy-loss spectroscopy (SPHREELS) (see Methods). The scattering geometry is sketched in Figure 1a. The scattering plane was chosen to be parallel to the [100]-direction of STO(001), as indicated in Figure 1b and c. This would allow probing the dynamic response of the system along the high-symmetry $\overline{\Gamma}-\overline{X}$ direction of the surface Brillouin zone (SBZ). Figure 1d shows the spin-resolved spectra recorded in the superconducting state of the sample and using an incident electron beam energy $E_i = 4.07$ eV. The spectra were recorded at the $\overline{\Gamma}$-point of SBZ. Beside the so-called zero loss peak at the energy-loss $\hbar\omega = 0$, one observes several features as a result of the excitation of several collective modes. The peaks with lower intensity at $\hbar\omega = 11.8$, 20.5, 24.8, and 36.7 meV represent the various phonon modes of the FeSe film itself.[23-25] More obviously the so-called Fuchs−Kliewer (FK) phonon modes of the underlying STO substrate can also be recognized at the loss energies $\hbar\omega = 59.3$ and 94.5 meV.[26,27]

Generally the spectral function $\mathcal{S}(q, \omega)$ reflects the dynamic response of the collective charge excitations in the system. This quantity is proportional to the imaginary part of the dynamic charge susceptibility $\mathfrak{Im}\chi(q, \omega)$.[28-30] The most interesting observation here is that $\mathcal{S}(q, \omega)$ depends strongly on the spin. The spin asymmetry $A = (I_{|+\rangle} - I_{|-\rangle})/(I_{|+\rangle} + I_{|-\rangle})$ is shown in the lower part of Figure 1d. Here $I_{|+\rangle}$ and $I_{|-\rangle}$ denote the intensity of the scattered electrons when the incoming electron's spin is parallel and antiparallel to $\hat{n}$, respectively.

In order to shed light on the origin of the observed spin asymmetry, its dependency on the physical variables, e.g., temperature, incident energy, and wavevector transfer q, was measured, and the results are summarized in Figure 2. Data presented in Figure 2a clearly demonstrate that the spin
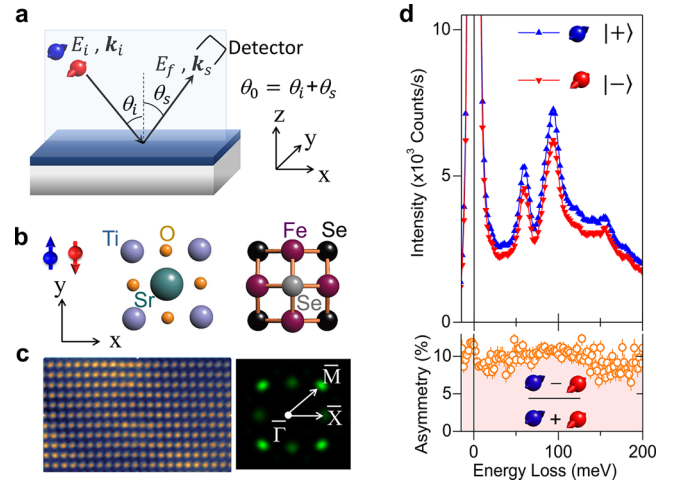
Figure 1. Evidence of a large SOC in FeSe ML on STO. (a) The scattering geometry used for probing the dynamic charge response. The electrons are represented by the blue and red balls. Their spin in the laboratory frame is shown by the red and blue arrows. The incident energy and wavevector are denoted by E_i and $\vec{k}_i$, respectively. The energy and the wavevector after the scattering event are given by E_f and $\vec{k}_s$, respectively. The laboratory frame is depicted by black arrows with x, y, and z labels. The incident and outgoing angles are called θ_i and θ_s. The total scattering angle is θ_0 and was set to 80°. (b) The top view of STO(001) and the FeSe(001) film. The spin polarization of the beam is either parallel or antiparallel to the y-axis that is the [010]-direction of the STO(001) surface. These spin states are called $|+\rangle$ and $|-\rangle$, respectively. (c) Atomically resolved scanning tunneling microscopy topography image of the FeSe surface, showing the atomic resolution of the topmost Se atoms, indicated by the gray balls in (b). The field of view is 7×4.5 nm^2. The constant current topography image was recorded at $T = 0.9$ K and using a tunneling current of 180 pA and a bias voltage of 1.0 V. The corresponding reciprocal lattice is shown on the right side. The $\overline{\Gamma}$-point represents the SBZ center, and the $\overline{X}$- and $\overline{M}$-points represent the edges of SBZ. (d) Blue upward and red downward triangles represent the experimental spectra recorded for the spin of the incoming beam being parallel and antiparallel to the y-axis, respectively. The open circles denote the spin asymmetry $A = (I_{|+\rangle} - I_{|-\rangle})/(I_{|+\rangle} + I_{|-\rangle})$. The spectra were recorded at the specular geometry, i.e., the wavevector of $q = 0$, at the $\overline{\Gamma}$-point. The error bars represent the statistical uncertainties.

asymmetry does not depend on temperature. In both superconducting and normal states one observes a value as large as 11%. This observation indicates that the spin asymmetry is not related to the superconducting (or magnetic) phase transition and is due to the intrinsic SOC of the system. Note that in the scattering of spin-polarized electrons from surfaces there are two main mechanisms, which can lead to the observation of a spin asymmetry, i.e., (i) exchange scattering and (ii) spin−orbit scattering. The exchange-induced spin asymmetry is usually observed when spin-polarized electrons are scattered from ferromagnetic surfaces with a spontaneous magnetization. The asymmetry vanishes when the long-range magnetic order disappears, e.g., at temperatures above the Curie temperature.[31] In contrast, spin−orbit scattering is not correlated with magnetic ordering, and hence spin asymmetry associated with this mechanism is temperature independent.[32] Next we check the dependence of the spin asymmetry on the incident beam energy E_i. Generally for very low incident energies ($E_i < 3$ eV) the intensity may be influenced by the
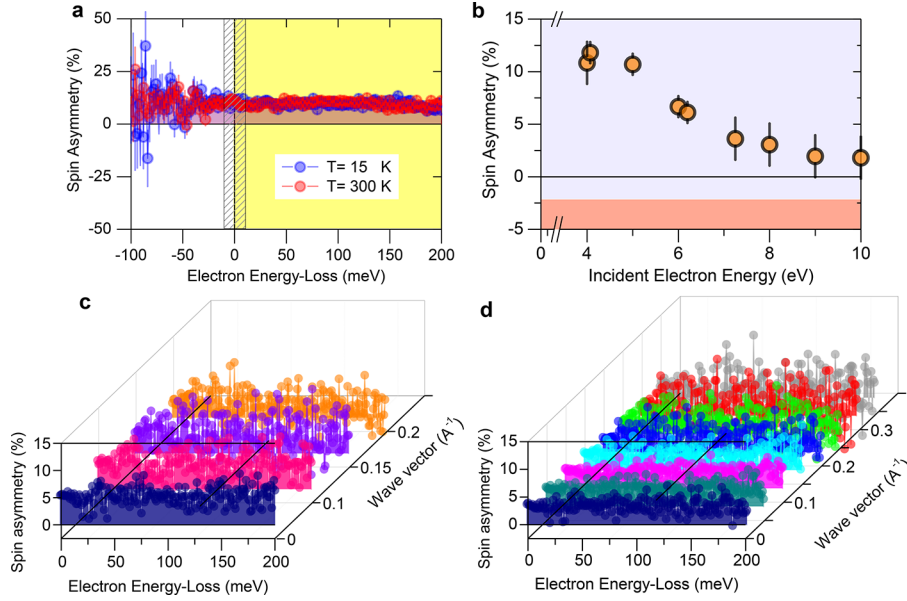
Figure 2. SOC as the origin of the observed spin asymmetry. (a) Spin asymmetry measured below (T = 15 K) and above (T = 300 K) the superconducting transition temperature. The data are recorded at an incident beam energy of 4.07 eV and at the specular geometry (q = 0). The error bars represent the statistical uncertainties. (b) Spin asymmetry as a function of the incident beam energy. The error bars represent the systematic uncertainties. (c, d) The pattern of the spin asymmetry over the energy loss for different values of wavevector along the $\overline{\Gamma}-\overline{X}$ direction. The graphs represent the spin asymmetry of the spectral function $S(q, \omega)$. The data shown in (c) are recorded at an incident beam energy of 6.0 eV, and those shown in (d) are recorded at 7.25 eV.

space charge effects. On the other hand for incident energies higher than 12 eV the intensity is determined by the multiple scattering and electron diffraction processes. Hence, the relevant energy window would be between 3 and 11 eV. Such data are presented in Figure 2b. For this set of measurements first the incident and scattered beam angles were fixed to $\theta_i = \theta_s = 40°$ (see Figure 1a). The incident beam energy E_i was precisely defined, and the electrons with the final energy $E_f = E_i \pm \delta E$ were collected. Here δE represents the energy width of the elastic scattering (the hatched area in Figure 2a). In order to make sure that all the elastically scattered electrons are collected, we recorded the intensity for δE = 8 meV (this value is two times the energy resolution). The spin asymmetry shows a strong dependence on the incident beam energy and exhibits a maximum near 4 eV. As the next physical variable we check the dependence of the spin asymmetry on q. Spectra recorded for different values of q near the zone center (in the vicinity of the $\overline{\Gamma}$-point) indicate that the spin asymmetry does not depend on q. This is demonstrated in Figure 2c and d, where the spin asymmetry recorded for different values of q is presented. The data shown in Figure 2c were recorded with an incident beam energy of E_i = 6.0 eV, and those in Figure 2d were recorded with E_i = 7.25 eV. A careful inspection of the data shown in Figure 2c and d indicates that although the spin asymmetry depends strongly on E_i, it does not depend on q. Note that the spectra are all measured along the main symmetry $\overline{\Gamma}-\overline{X}$ direction of SBZ. Along this direction the electronic structure of FeSe is rather uniform. The q-independent dynamic charge response means that the collective excitations associated with these charges exhibit a rather weak in-plane dispersion relation. This is not surprising since the response function is mainly governed by optical phonons (the FK modes of the STO substrate as well as the FeSe optical phonons) which show a negligible dispersion. The contributions of collective electronic excitations to the

response function are (i) broadening of the elastic peak (known as Drude contribution) and (ii) screening the response of the FK phonons by additional broadening and, under some circumstances, a blueshift of their excitation frequency. In other words the observed FK modes are hybridized modes of the collective excitations of both electronic and ionic degrees of freedom of the whole system. It is important to notice that in SPHREELS the probing particles are electrons, which interact with the total charge distribution of the sample and not with the electronic charge distribution only (see also the discussion in ref 33). The strong E_i-dependence of spin asymmetry and its q-independence are unambiguous evidence that the observed spin asymmetry is originating from a substantially large SOC at the surface. We note that the most straightforward way to confirm that the observed spin asymmetry has its origin in the spin−orbit scattering is to perform an experiment in which the polarization vector of the incident electron beam is inside the scattering plane, i.e., using a transversally spin-polarized beam. However, such an experiment with the desired energy and momentum resolution is not practically feasible (see Note I and Figure 1S of the Supporting Information). Additional compelling evidence confirming the spin−orbit origin of the spin asymmetry comes from two other experiments: (i) experiments with a linearly polarized light and (ii) experiments with different total scattering angles $\theta_0 = \theta_i + \theta_s$. Both experiments clearly indicate that the observed spin asymmetry must be due to a large SOC (see Note II and Figures 2S and 3S in the Supporting Information).

DISCUSSION

It is well known that when a beam of spin-polarized slow electrons is scattered from a free atom with a large atomic number, and consequently a large SOC, the scattering cross-section can be spin dependent.[34,35] The effect is understood

based on the fact that due to the relativistic effects the electrons with different spins feel different scattering potentials, while scattered off the atom.[35] The same phenomenon has also been observed when such a beam is scattered from a surface, i.e., an array of atoms ordered in a two-dimensional fashion.[32,35−39] The effect is attributed to the intrinsic SOC of the involved atoms. In a quantum mechanical description all the states in the image potential as well as those in the crystal must be represented by their spinors, when describing the scattering process. The matching of plane wave spinors in the vacuum above the surface, Bloch spinors inside the sample, and surface spinors at the interface become spin dependent if SOC is sufficiently large in the system.[32,36] This rather simple description can explain the spin-dependent scattering in the elastic regime very well.[36−39] As a consequence of the broken translation symmetry at the surface, the largest effect is observed when the spin of the incoming electron beam is parallel and antiparallel to $\hat{n}$ (the spin asymmetry is maximum in this case). The value of the spin asymmetry depends only on the sum over all the possible scattering phase shifts caused by the involved atomic orbitals, which, in turn, depend on the incident energy E_i.[35,36,40] The spin asymmetry does not depend on q, as long as the total scattering angle θ_0 is kept constant. Experiments performed at larger scattering angles indicate that the spin asymmetry decreases for larger values of θ_0. It even changes the sign for some values of E_i (see Figure 3S and the corresponding discussion in Supporting Note II). More importantly, the maximum asymmetry is expected for a longitudinally spin-polarized beam in which the direction of spin polarization vector is parallel or antiparallel to the scattering's plane normal vector $\hat{n}$[35,36,40] (see Note III of the Supporting Information for a simplified explanation).

Besides the elastic part, an even more interesting part is the energy-loss region, where the collective excitations of the system show up. We, therefore, carefully analyzed the spin asymmetry as a function of electrons' energy in the final state after scattering E_f, while keeping the energy of the incident electrons constant. The data are presented in Figure 3. For this set of measurements we first optimized the incoming beam at a given energy E_i and probed the spin asymmetry of the elastic scattering at $E_f = E_i \pm \delta E$. The results are shown by the filled circles in Figure 3. Then for each value of E_i we probed the spin asymmetry as a function of E_f over an energy range for which we could obtain reasonable count rates. The experiment was performed for various values between 4 and 9 eV. The results clearly demonstrate that the spin asymmetry versus scattered beam energy follows the same trend as that of the elastic scattering for different energies. For example for the electrons with the incident energy of $E_i = 4$ eV the asymmetry decreases when decreasing E_f from 4 to 3.5 eV. However, for the higher incident energies the spin asymmetry gradually increases when moving toward lower values of E_f. This means that the observed spin asymmetry in the energy loss region has the same origin as that of the elastic scattering. In simple words electrons contributing to the surface loss processes are then affected by the SOC potential before they are finally scattered out. In the limit of small energy losses ($\hbar\omega = E_i − E_f \ll E_i$) the spin asymmetry is almost entirely determined by the incident energy E_i.

Yet the question whether or not the dynamic charge response depends on the spin of the incident electron remains unanswered. In order to answer this question and shed light onto the origin of the observed spin asymmetry, we developed
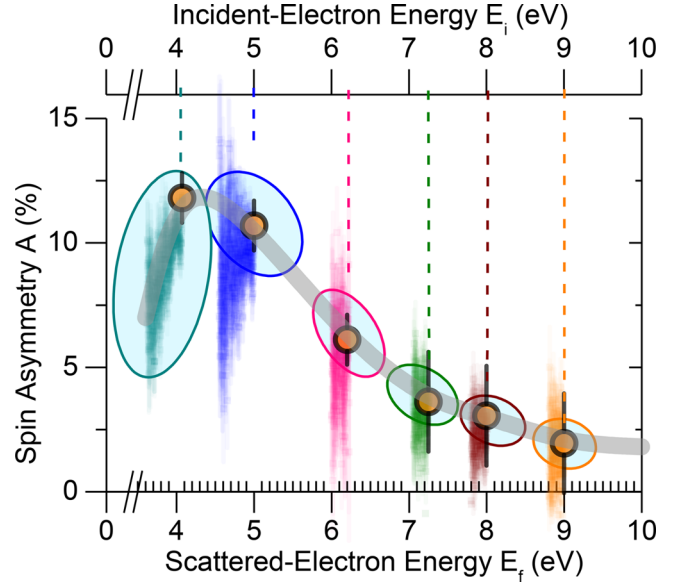

Figure 3. Dependence of the spin asymmetry on the energy of the scattered beam. Spin asymmetry A versus scattered beam energy E_f when the incident beam energy E_i is kept constant. For each set of data the energy of the incident beam E_i is also shown using the top axis; $E_i = 4$ (teal color), 5 (blue color), 6.2 (red color), 7.3 (green color), 8 (brown color), and 9 (orange color) eV. The filled circles represent the elastic scattering, i.e., cases in which $E_i = E_f$. The gray thick curve is a guide to the eye and describes the E_i-dependence of A shown in Figure 2b. The data indicate that the E_f-dependence of A is the same as its E_i-dependence. The error bars represent the systematic uncertainties.

a model to simulate the SPHREEL spectra. The simulation is based on the scattering theory of spin-polarized electrons from a surface with a nonnegligible SOC. The theory is an extension of the original theory of Evan and Mills[41−43] for unpolarized electrons. In our modeling of the scattering event and in the calculation of the scattering cross-section we further account for SOC and spin-dependent electron reflection, in addition to the Hartree or Coulomb scattering (see Methods for details). Our theory indicates that the observed spin asymmetry is almost entirely due to the spin-dependent electron reflection from the surface, which in turn is a result of SOC. In order to verify this hypothesis, we simulated the SPHREEL spectra using the values of spin-dependent reflection coefficient measured for the elastic scattering (data shown in Figure 2b). The results of simulation for two different values of E_i are shown in Figure 4 together with the experimental spectra. Our theory is able to perfectly reproduce the experimental spectra. In the simulation we considered a system composed of an atomic layer of FeSe (Se−Fe−Se trilayer structure) on 17 unit cells of charge-free insulating STO(001) on top of a semi-infinite Nb-STO(001). In this model the Fe plane in FeSe ML is placed at $d_{FeSe} = 0.43$ nm above the insulating STO(001) surface.[44] Only in this way both the peak position and amplitude of the excitations associated with the FK modes agree with those measured experimentally. The discovery of a charge depletion layer below the FeSe layer has been discussed in detail in ref 33. As discussed in ref 33, the presence of a charge depletion layer, which is due to a considerably large charge transfer from the Nb-doped STO to the FeSe film, has several serious consequences on the system. One of the consequences is that it generates a rather large electric field and
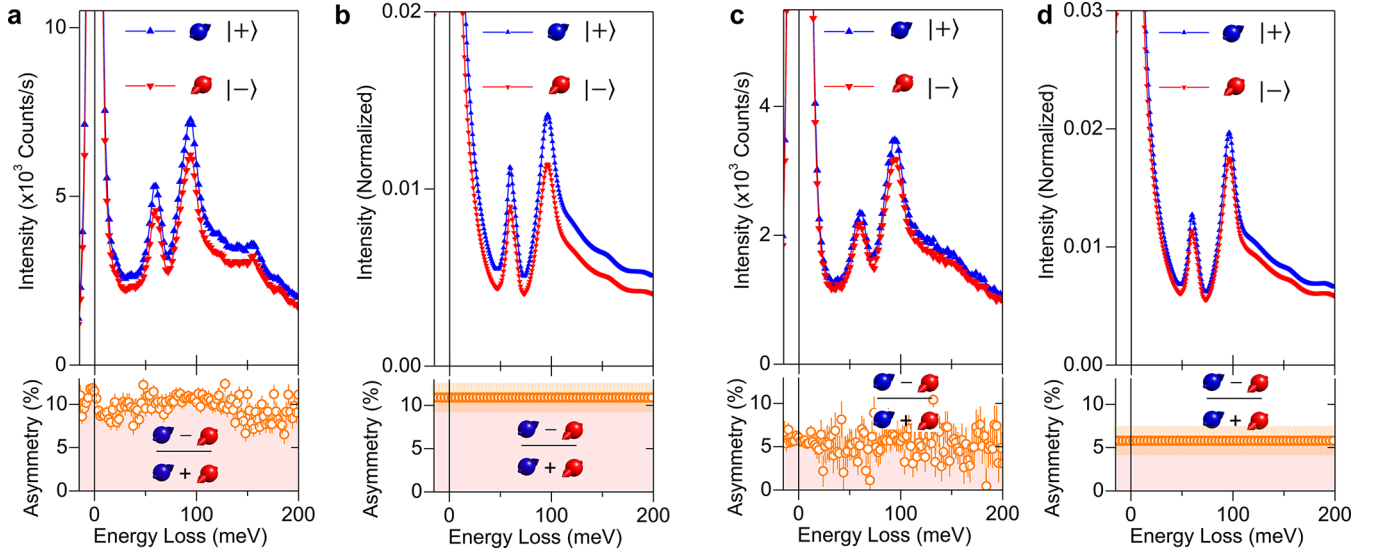
Figure 4. Spin dependence of the dynamic charge response. (a and b) The measured and simulated SPHREEL spectra at an incident electron energy of E_i = 4.07 eV. (c and d) The measured and simulated SPHREEL spectra at an incident electron energy of E_i = 6.0 eV. Blue upward and red downward triangles represent the spectra recorded or simulated for the incoming spin states of |+⟩ and |−⟩ (spin polarization parallel and antiparallel to the y-axis in Figure 1a), respectively. The open circles denote the spin asymmetry $A = (I_{|+⟩} − I_{|−⟩})/(I_{|+⟩} + I_{|−⟩})$. All the experimental spectra are recorded at T = 15 K in the superconducting state of the sample and at the specular geometry, i.e., the wavevector of q = 0, at the $\bar{\Gamma}$-point. The error bars in spin asymmetry represent the statistical uncertainties.

band bending near and below the interface. As a rule of thumb one may simply divide the value of the total band bending, probed by the experiment (2.1 V), by the depletion layer thickness (6.5 nm). This results in an electric field on the order of 0.3 GV/m. Such a large electric field greatly influences the electronic states in the FeSe ML and boosts SOC at and near the surface region. The effect is very similar to the Rashba and Dresselhaus effects observed for semiconductor quantum-well states and two-dimensional electron gases formed at the semiconductor surfaces and interfaces.[2]

Experiments performed on bulk Fe-based superconductors[22,45] have shown that the Fe atoms possess a nonnegligible SOC. In the present case one deals with only one unit cell FeSe grown on a substrate. As a result of unquenched orbitals, one would expect a sizable SOC. Moreover, the FeSe monolayer is subject to a rather strong electric field as a result of the charge transfer and the dielectric depletion layer; we conclude that the observed large SOC in this system is, therefore, an additive effect. It includes the SOC resulting from the unquenched orbitals as well as the electric field induced SOC, as discussed above. We would like to emphasize that the observed large SOC is associated with the whole FeSe/STO system and is not present at the bare STO(001) surface (see Figure 4S of the Supporting Information).

Generally, SOC in solids manifests itself as spin-dependent effects in the bandstructure, e.g., spin-split bands at some part of the BZ, and only in simplified cases it might be represented as a parametrized Hamiltonian. One may, however, provide an estimation of SOC in a comparative way. To this end, we performed experiments on FeSe(001), Cu(001), Pd(001)−O, W(110), and Ir(001) surfaces. We also compare the results to those of Bi$_2$Se$_3$(0001), measured recently.[30] It was found that the FeSe(001) surface exhibits a negligible spin asymmetry, similar to the Cu(001) and Pd(001)−O surfaces, which are know to have a small SOC (see Figure 5S in the Supporting Information). A measurable asymmetry was only observed for W(110), Bi$_2$Se$_3$(0001), and Ir(001) surfaces (82%, 44%,[30] and

68%, respectively) on which the SOC is expected to be large. It was found that for the measurements performed at the total scattering angle of θ_0 = 80 the W(110) surface shows the largest spin asymmetry of about 82% at an incident energy of about E_i = 9 eV (the corresponding experimental data are provided in Figure 6S of the Supporting Information). Compared to the value of 11% observed for the FeSe/STO system, at the incident energy of E_i = 4−5 eV one would conclude that the SOC strength in FeSe/STO is by a factor of 8 smaller than that of W(110) and by a factor of 4 smaller than that of Bi$_2$Se$_3$(0001).[30] We note that this comparison provides only a rough estimation of the SOC strength. It is important to emphasize that experiments on the FeSe(001) surface[23] showed a small spin−orbit spin asymmetry, meaning that the effect should be attributed to the whole FeSe/STO system (compare Supporting Figure 5Sc and d).

In most of the ARPES experiments performed on the FeSe/STO system the attention has been paid to the bands near the Fermi level. We note that SOC may influence the states far below the Fermi level. Moreover, the consequence of SOC on the electronic bands is not always a simple Rashba type of splitting. The effect may be much more complex and influence the deeper bands. The spin−orbit mechanism mentioned above refers to the general Rashba−Dresselhaus SOC and not the simple splitting of a spin-degenerate band. An evidence for a large SOC from the ARPES experiments, confirming our statement, might be the shape of the gap function. It has been shown that the angular dependence of the gap function can only be explained if SOC is large (larger than the mismatch between the electron pockets).[20]

Generally, topological properties and SOC are tightly interconnected. It has been discussed that the appearance of a topological phase in FeSe/STO is associated with (i) a trivial bandgap in the electronic band structure near the $\bar{M}$-point, (ii) the parity-broken coupling at the interface, and (iii) a sufficiently large SOC.[46,47] As a mater of fact experimental evidence of topological states in an FeSe ML has been reported

by scanning tunneling spectroscopy.[47,48] However, the attribution of the observed peaks in the tunneling spectra to the topological states has entirely been based on the first-principles calculations. An important piece of this puzzle, i.e., a direct experimental probe of SOC, has been missing. This is now provided by our experimental results. Since the effect is an interfacial effect, we anticipate that it should be present in other similar combinations of van der Waals MLs with dielectric substrates.

The presence of such a large SOC can have serious consequences on the phenomenon of high-temperature superconductivity in FeSe/STO. In the following we comment on such possible consequences.

The observation of the so-called replica bands has been considered as an indication of a phonon-mediated super-conductivity in FeSe/STO.[15,19,49−53] This suggestion is merely based on probing the quasiparticle bands, and no evidence has been reported by probing the phonons. On the other hand it has also been discussed that the pairing mechanism can be of unconventional nature and be mediated by spin fluctuations.[54,55] The signature of such a coupling has experimentally been observed by means of tunneling spectroscopy experiments.[27,56] Moreover, it has been suggested that a cooperative effect of several bosonic excitations may be the main reason for such a high transition temperature of this system.[52,57,58] Besides the mechanisms discussed above, it has theoretically been shown that nematic fluctuations alone promote a highly degenerate pairing state, in which both s-wave and d-wave symmetries are equally favored. However, considering both the effect of nematic fluctuations and SOC in the absence of inversion symmetry, an s-wave state is favored.[20] Interestingly, if nematic fluctuations and SOC are strong enough so that they overcome the mismatch between the electron pockets near the $\bar{M}$-point, the gap function measured in the experiment can be well reproduced by the theory.[20] Our results clearly demonstrate that SOC is large. This fact together with the observation of spin fluctuations, we have reported earlier,[27] may lead to the conclusion that the pairing symmetry in this system should be of $s_{\pm}$ character (see for example ref 59).

CONCLUSION

While probing the dynamic charge response of the FeSe superconducting ML on STO by means of SPHREELS, we observed that the scattering cross-section is strongly spin dependent. The observed spin asymmetry is attributed to a large SOC at and near the surface region. This large SOC, which very likely originates from the d orbitals of the Fe atoms[20] and the presence of a dielectric depletion layer below the FeSe ML, has several consequences on the properties of the system. One of the important consequences is the formation of topological states. The depletion layer is a result of charge transfer from the Nb-STO into the FeSe layer, which leads to a band bending and the generation of an electric field at the interface.

Since the charge transfer, the formation of a depletion layer at the interface, and the associated electric field are general phenomena, we anticipate that the observed effect is also general and shall be observed for other Fe-based super-conducting monolayers brought in contact with STO or other dielectric oxides. This would allow an interfacial engineering of the superconducting states by growing ML iron chalcogenides or other HTSC on dielectric oxides. Realization of topological states in superconducting MLs would provide a platform for

investigation and realization of Majorana states in, structurally, very simple systems.

In addition to the facts mentioned above, our results suggest that the superconductivity in FeSe ML is very likely of $s_{\pm}$ nature and, therefore, shed light on the long-standing question regarding the nature of the superconducting order parameter and the pairing symmetry in this system.

METHODS

Experiments. *Sample Preparation and Characterization.* All the sample growth and characterizations were performed under ultrahigh-vacuum conditions. FeSe ML was grown by means of the molecular beam epitaxy technique on the Nb-doped STO(001) substrates in a separate chamber.[27,60] The Nb-doping level was 0.6%. Prior to the film growth, the substrate was annealed at temperatures up to about 1000 °C and was then etched by a selenium flux for 20 min in. The sample was kept at the elevated temperature for 30 min and then was gradually cooled down to 480 °C. Fe and Se were co-deposited with a growth rate of 0.059 ML/min at 480 °C at a flux ratio of Fe:Se ≡ 1:10. The sample was postannealed at 500 °C right after the deposition for several hours to ensure a good morphological quality. This also ensures desorption of the residual Se atoms on the surface. The film growth was monitored by reflection high-energy electron diffraction.

For the further measurements, the sample was transferred using an ultrahigh-vacuum suitcase to the scanning tunneling microscopy and spin-polarized high-resolution electron energy-loss spectroscopy chambers.

The morphological and electronic properties were investigated by means of scanning tunneling microscopy.[27] Our samples show a superconducting gap of about $\Delta = 11 \pm 3$ meV at a temperature of about 0.9 K.

Spin-Polarized High-Resolution Electron Energy-Loss Spectroscopy. The dynamic response of the samples was investigated by means of spin-polarized high-resolution electron energy-loss spectroscopy.[61]

A spin-polarized monochromatic electron beam with an energy resolution between 4 and 11 meV was used.[61,62] The spin-polarized electron beam is generated by photoemission from a strained GaAsP photocathode. In order to observe maximum spin asymmetry, a longitudinally spin-polarized beam was used, meaning that the polarization vector of the incoming electron beam was either parallel or antiparallel to the scattering's plane normal vector $\vec{n}$ (for a simplified explanation see Note III of the Supporting Information). For the parallel case we call these incoming spin states |+⟩ and for the antiparallel case we call them |−⟩. The degree of the beam polarization was estimated by performing spin-polarized elastic reflectivity from a W(110) single crystal, resulting in a value of about 72 ± 5%. The total scattering angle, i.e., the angle between the incident and the scattered beam, was kept constant ($\theta_0 = 80°$). The scattering intensity was recorded simultaneously for the two possible spin polarizations of the incoming electron beam |+⟩ and |−⟩. This means that first the scattering geometry was adjusted, and then the intensity of the scattered electrons was measured after energy analysis. When recording the intensity of the scattered beam, two values for the intensity were recorded: one for electrons with |+⟩ spin state and the other one for electrons with |−⟩ spin state. Changing the incoming spin state from |+⟩ to |−⟩ was realized by reversing the helicity of the laser beam used for the excitation and emission of the spin-polarized electrons from the photocathode. The scattered electron beam was energy analyzed without any further spin analysis.

In order to collect the spectra in off-specular geometry at a certain wavevector transfer q, the scattering geometry was adjusted to realize the required wavevector transfer. The in-plane wavevector transfer is given by $q = k_i \sin \theta_i - k_s \sin(\theta_0 - \theta_i)$, where k_i (k_s) is the magnitude of the wavevector of the incident (scattered) electrons and θ_i (θ_0) is the angle between the incident beam and sample normal (the scattered beam). Different wavevector transfers were achieved by changing the scattering angles, i.e., by rotating the sample about its

main axis. In the experiments θ_0 was kept at 80°. The spectra were recorded along the $\bar{\Gamma}-\bar{X}$ direction of the surface Brillouin zone. The wavevector resolution of the experiment is given by $\Delta q = \sqrt{2mE_i}/\hbar[\cos\theta_i + \cos(\theta_0 - \theta_i)]\Delta\theta_i$. E_i denotes the energy of the incident beam and $\Delta\theta_i$ depends on the spectrometer design (in our case $\Delta\theta_i = 2°$). The resolution of the spectrometer in momentum space is about 0.03 Å^{-1}.

Theory. *Theory of Spin-Dependent Scattering Cross-Section.* We define $|m\rangle$ and $|n\rangle$ as many-body states of the sample with energies E_m, E_n, and $|i\rangle$ and $|f\rangle$ as initial and final states of the electron with energies E_i and E_f. The general definition of the differential scattering cross-section is given by[63]

$$\frac{d^2S}{d\Omega d\hbar\omega} = \left(\frac{2\pi}{\hbar}\right)^4 m_e^2 \frac{k_s}{k_i} \sum_{mn} \frac{e^{-E_m/k_B T}}{Z} |\langle n, f|\hat{T}(E_m + E_i)|m, i\rangle|^2$$
$$\times \delta(E_m + E_i - E_n - E_f) \tag{1}$$

where m_e is the electron mass, $k_i = |\vec{k}_i|$ and $k_s = |\vec{k}_s|$ are the norms of the three-dimensional wavevectors of the incident and scattered electron, respectively, k_B is the Boltzmann constant, $Z = \sum_m e^{-E_m/k_B T}$ is the partition function, and $\hbar\omega = E_i - E_f$ is the energy loss of electrons during the scattering process. $\hat{T}(E)$ is the many-body t-matrix given by $\hat{T}(E) = \hat{V} + \hat{V}(E + i0 - \hat{H})^{-1}\hat{T}(E)$ with $\hat{H}$ the Hamiltonian of the sample and $\hat{V}$ the interaction energy of the incident electron with the sample. We use the first-order (Born) approximation, $\hat{T}(E) \approx \hat{V}$.

The interaction energy of the incident electron with the sample is written as $\hat{V} = \hat{V}_H + \hat{V}_{SOC}$, ignoring the exchange–correlation term. $\hat{V}_H$ is the Hartree energy, i.e., the electrostatic interaction with the charge density in the sample. We define the total charge density operator $\hat{\rho}(\vec{R})$ given in units of Coulomb per unit volume, where $\vec{R}$ is a three-dimensional position vector. For the given geometry it can be decomposed into the in- and out-of-plane components $\vec{R} = (\vec{r}, z)$. Here z represents the coordinate normal to the surface, and the sample is placed in the x–y plane at $z < 0$ (the surface is located at $z = 0$). Note that $\hat{\rho}(\vec{R})$ includes both negative and positive charges in the sample. This operator acts on the many-body states with matrix elements $\langle n|\hat{\rho}(\vec{R})|m\rangle$. The Hartree energy is

$$\hat{V}_H(\vec{R}) = e\int d\vec{R}' \frac{\hat{\rho}(\vec{R}')}{4\pi\epsilon_0|\vec{R} - \vec{R}'|}\sigma_0 \tag{2}$$

where σ_0 is the identity matrix in spin space, since the Hartree potential conserves the spin of the electron during the scattering process. $\hat{V}_{SOC}$ is the spin–orbit interaction given by

$$\hat{V}_{SOC}(\vec{R}) = \frac{e\hbar}{4m_e^2 c^2}\vec{\sigma}\cdot[\hat{\vec{E}}(\vec{R}) \times \vec{p}] \tag{3}$$

Here $\vec{\sigma}$ is the vector of Pauli matrices, $\hat{\vec{E}}(\vec{R}) = -\vec{\nabla}\hat{V}_H(\vec{R})/e$ is the electric field due to the charge distribution $\hat{\rho}(\vec{R})$, and $\vec{p} = -i\hbar\vec{\nabla}$ is the momentum operator.

In the next step we introduce the wave functions of the incident and scattered electrons, taking into account spin-dependent reflection coefficients

$$\psi_i(\vec{R}) = N_i e^{i\vec{k}_i\cdot\vec{r}}(\vec{i}\,e^{ik_i^z z} + \mathcal{R}\vec{i}\,e^{-ik_i^z z})\theta(z) \tag{4a}$$

$$\psi_s(\vec{R}) = N_s e^{i\vec{k}_s\cdot\vec{r}}(\vec{s}\,e^{ik_s^z z} + \mathcal{R}\vec{s}\,e^{-ik_s^z z})\theta(z) \tag{4b}$$

N_i and N_s are normalization factors, $\theta(z)$ denotes the Heaviside step function, $\vec{i}$ and $\vec{s}$ are two-component vectors representing the initial and final states in some spin-1/2 basis (for instance the $\{|+\rangle, |-\rangle\}$ basis), and $\mathcal{R}$ is the reflection matrix expressed in the same basis. For definiteness, we note that a matrix $\mathcal{R}$ expressed in the usual basis $\{|\uparrow\rangle, |\downarrow\rangle\}$ with the spin quantization axis along z can be rotated to a basis with quantization axis along a direction defined by the polar and azimuthal angles (ϑ, φ) by means of the unitary transformation

$$\mathcal{U}^\dagger\mathcal{R}\mathcal{U} \quad \text{with} \quad \mathcal{U} = \begin{pmatrix} \cos\dfrac{\vartheta}{2} & -\sin\dfrac{\vartheta}{2} \\ \sin\dfrac{\vartheta}{2}e^{i\varphi} & \cos\dfrac{\vartheta}{2}e^{i\varphi} \end{pmatrix}. \quad \text{The } \{|+\rangle, |-\rangle\} \text{ basis}$$

corresponds to $(\vartheta, \varphi) = (\pi/2, \pi/2)$ (see the Cartesian coordinates in Figure 1a). Inserting eqs 4 and 2 in eq 1, we find that the scattering cross-section including only the Hartree term can be written as

$$\frac{d^2S_H}{d\Omega d\hbar\omega} = \left(\frac{2\pi}{\hbar}\right)^4 m_e^2 \frac{k_s}{k_i}\left(\frac{e}{2\epsilon_0 q}\right)^2 (N_s N_i)^2$$
$$\times \left|\frac{\vec{s}^\dagger\cdot\vec{i}}{q + iq_z^-} + \frac{\vec{s}^\dagger\cdot(\mathcal{R}\vec{i})}{q + iq_z^+} + \frac{(\mathcal{R}\vec{s})^\dagger\cdot\vec{i}}{q - iq_z^+} + \frac{(\mathcal{R}\vec{s})^\dagger\cdot(\mathcal{R}\vec{i})}{q - iq_z^-}\right|^2 \times$$
$$\int_{-\infty}^0 dz dz' S(\vec{q}, z, z', \omega)e^{-q|z+z'|} \tag{5}$$

where $q_z^\pm = k_s^z \pm k_i^z$, $S(\vec{q}, z, z', \omega) = \frac{1}{Z}\sum_{mn} e^{-E_m/k_B T}\langle m|\hat{\rho}(-\vec{q}, z)|n\rangle\langle n|\hat{\rho}(\vec{q}, z')|m\rangle\delta(\hbar\omega + E_m - E_n)$ and $\vec{q}$ is a two-dimensional vector with $|\vec{q}| = q$.

Likewise, the spin–orbit cross-section can be expressed as

$$\frac{d^2S_{SOC}}{d\Omega d\hbar\omega} = \left(\frac{2\pi}{\hbar}\right)^4 m_e^2 \frac{k_s}{k_i}\left(\frac{e}{2\epsilon_0 q}\right)^2 (N_s N_i)^2 |\alpha|^2$$
$$|(\mathcal{G}_+)^{+-}q(k_i^x - ik_i^y) + (\mathcal{G}_-)^{+-}(q_x - iq_y)ik_i^z$$
$$- (\mathcal{G}_+)^{-+}q(k_i^x + ik_i^y) - (\mathcal{G}_-)^{-+}(q_x + iq_y)ik_i^z$$
$$+ [(\mathcal{G}_+)^{++} - (\mathcal{G}_+)^{--}](q_x k_i^y - q_y k_i^x)|^2$$
$$\times \int_{-\infty}^0 dz dz' S(\vec{q}, z, z', \omega)e^{-q|z+z'|} \tag{6}$$

where $(\mathcal{G}_\pm)$ is given by

$$(\mathcal{G}_\pm)^{\sigma\sigma'} = \frac{s_\sigma^* i_{\sigma'}}{q + iq_z^-} \pm \frac{s_\sigma^*(\mathcal{R}_{\sigma'\sigma}i_{\sigma'} + \mathcal{R}_{\sigma'\bar{\sigma}}i_{\bar{\sigma}})}{q + iq_z^+}$$
$$+ \frac{(\mathcal{R}_{\sigma\sigma}^* s_\sigma^* + \mathcal{R}_{\sigma\bar{\sigma}}^* s_{\bar{\sigma}}^*)i_{\sigma'}}{q - iq_z^+}$$
$$\pm \frac{(\mathcal{R}_{\sigma\sigma}^* s_\sigma^* + \mathcal{R}_{\sigma\bar{\sigma}}^* s_{\bar{\sigma}}^*)(\mathcal{R}_{\sigma'\sigma}i_{\sigma'} + \mathcal{R}_{\sigma'\bar{\sigma}}i_{\bar{\sigma}})}{q - iq_z^-} \tag{7}$$

Here $\alpha = -i\hbar^2/(4m_e^2 c^2)$, $\bar{\sigma} \equiv -\sigma$, and $\mathcal{R}_{\sigma\sigma'}$ represent the reflection coefficients when an electron with a spin σ is impinged onto the sample and an electron with spin σ' is detected in the final state after the scattering event.

Equations 5 and 6 provide a description for the scattering intensities for any possible spin directions of the incoming and scattered beam, when the Hartree and SOC terms are treated separately. However, the quantities $\mathcal{R}_{\sigma\sigma'}$ are not known in practice. In order to overcome this problem, simplifications are needed. As it is apparent from eq 6, the spin–orbit cross-section is by a factor $\sim|\alpha q k_i|^2$ smaller than the Hartree cross-section, and hence its contribution to the intensity may be neglected. The Hartree contribution by itself should, in principle, conserve the spin during the scattering process. In such a scenario no spin asymmetry is expected. In order to account for the spin-dependent effects, one may assume that the reflection coefficients are spin dependent even for the case of Hartree scattering. In this case one would observe a spin asymmetry. This means that the role of SOC is to break the spin degeneracy and thereby lead to spin-dependent reflection coefficients.

Our analysis showed that, indeed, in this case the asymmetry caused by the Hartree term introduced in eq 5 does not depend, in first approximation, on q and $\hbar\omega$ and is given by (for an extended discussion see ref 64)

$$\frac{I_{|+\rangle} - I_{|-\rangle}}{I_{|+\rangle} + I_{|-\rangle}} \approx \frac{\mathcal{R}_{++}^2 - \mathcal{R}_{--}^2}{\mathcal{R}_{++}^2 + |\mathcal{R}_{+-}|^2 + |\mathcal{R}_{-+}|^2 + \mathcal{R}_{--}^2} \tag{8}$$

We define the quantities $|\mathcal{R}_{|+\rangle}|^2 = |\mathcal{R}_{++}|^2 + |\mathcal{R}_{+-}|^2$ and $|\mathcal{R}_{|-\rangle}|^2 = |\mathcal{R}_{--}|^2 + |\mathcal{R}_{-+}|^2$, which represent the intensity of the

scattered electrons when the spin of the incoming beam is of $|+\rangle$ and $|-\rangle$ character, respectively. Such quantities can be extracted from the spin-dependent elastic reflectivity data. The asymmetry strongly depends on the incident (scattered) energy as well as the scattering geometry, since $|\mathcal{R}_{|+\rangle}|^2$ and $|\mathcal{R}_{|-\rangle}|^2$ depend on these variables.

In our simulations we use exactly the same formalism introduced by Evan and Mills[41,42] and implemented by Lucas and Šunjić.[65−67] In order to account for the spin-dependent effects, we use reflection coefficients measured by the elastic reflectivity measurements (see below).

Simulation. Simulations of the spectra were performed by a numerical scheme based on the dipolar scattering theory. To calculate $P^{\mathrm{sl}}(\omega)$, we first calculate the single-loss probability

$$P(\omega) = \frac{e^2|\mathcal{R}_{|\sigma\rangle}(E_i)|^2}{4\pi\epsilon_0\hbar v_\perp}\frac{4}{\pi^2}\iint_\Omega \mathrm{d}^2q\,\frac{|\vec{q}|(v_\perp)^3}{[(\omega - \vec{q}\cdot\vec{v}_\parallel)^2 + (|\vec{q}|v_\perp)^2]^2}$$
$$\times \Im m\left[\frac{-1}{g(\vec{q},\,\omega) + 1}\right] \tag{9}$$

Here ϵ_0 is the vacuum permittivity, $\hbar$ is the reduced Planck constant, e is the electron charge, $v_\perp$ ($v_\parallel$) represents the perpendicular (parallel) component of the velocity of the incident electron, and $|\mathcal{R}_{|\sigma\rangle}| = |\mathcal{R}_{|+\rangle}|$ or $|\mathcal{R}_{|-\rangle}|$ denotes the reflection coefficient of electrons with the incoming spin state $|+\rangle$ or $|-\rangle$ and strongly depends on the incident energy E_i. The integration range Ω denotes the range of momentum covered by the exit and entrance slits of the monochromator and analyzer. We emphasize that in eq 9 $\vec{q}$ represents the two-dimensional vector of the momentum transfer parallel to the surface.

The most important entities in eq 9 are $|\mathcal{R}_{|\sigma\rangle}(E_i)|$ and the dielectric response function $g(\vec{q},\,\omega)$. The former is obtained from the experimental elastic reflection measured for different spin directions $|+\rangle$ and $|-\rangle$. For layered systems, such as our case, the latter can be related to the dielectric function of each individual layers $\varepsilon^p(q,\,\omega)$, where p is the layer index (for details see refs 65−68).

Equation 9 describes only the single-loss probability for an electron having a wavevector k_i and spin $|\sigma\rangle$ to be scattered from a semi-infinite slab system and loose the energy $\hbar\omega$ at $T = 0$ K. The multiple scattering events, the elastic peak, and temperature effects were included using the approach introduced by Lucas and Šunjić.[65−68]

We first construct a multislab system by considering one unit cell of FeSe on 17 unit cells (about 6.5 nm) of insulating STO on a semi-infinite Nb-doped STO(001) (a sketch of the structure is provided in Figure 7S of the Supporting Information). The dielectric function of each individual layer is then written in different contributions, i.e., (i) a frequency-independent background dielectric constant ε_∞^p, (ii) a phononic contribution $\varepsilon_{\mathrm{phonon}}^p$, and (iii) an electronic contribution $\varepsilon_{\mathrm{plasmon}}^p$:

$$\varepsilon^p(q,\,\omega) = \varepsilon_\infty^p + \varepsilon_{\mathrm{phonon}}^p + \varepsilon_{\mathrm{plasmon}}^p \tag{10}$$

We use the literature values of $\varepsilon_\infty^{\mathrm{FeSe}} = 15$ and $\varepsilon_\infty^{\mathrm{STO}} = 5.7$ for FeSe and STO, respectively.[69−72]

The phononic contribution to the dielectric function of each layer can be expressed in terms of different phonon contributions:

$$\varepsilon_{\mathrm{phonon}}^p = \sum_{j=1}^m \frac{Q_j\omega_{\mathrm{TO},j}^2}{\omega_{\mathrm{TO},j}^2 - \omega^2 - i\gamma_{\mathrm{TO},j}\omega} \tag{11}$$

where m is the number of all transverse optical (TO) phonon modes with the oscillator strength Q_j, which depends on the splitting between TO and longitudinal optical (LO) modes:

$$Q_j = \frac{\varepsilon_\infty}{\omega_{\mathrm{TO},j}^2}\frac{\prod_l(\omega_{\mathrm{LO},l}^2 - \omega_{\mathrm{TO},j}^2)}{\prod_{l\neq j}(\omega_{\mathrm{TO},l}^2 - \omega_{\mathrm{TO},j}^2)} \tag{12}$$

where $\omega_{\mathrm{TO},j}$ and $\omega_{\mathrm{LO},j}$ denote the frequency of the jth TO and LO phonon modes, respectively. $\gamma_{\mathrm{TO},j}$ and $\gamma_{\mathrm{LO},j}$ represent their corresponding damping.

In addition, we consider a Drude-like term in the dielectric function of each layer, in order to account for the contribution of the charge carriers:

$$\varepsilon_{\mathrm{plasmon}}^p = -\varepsilon_\infty\frac{\omega_{pl}^2 - i(\gamma_{pl} - \gamma_0)\omega}{\omega(\omega + i\gamma_0)} \tag{13}$$

where ω_{pl} denotes the plasma frequency associated with the charge carriers and is directly related to the carrier density n_c and carriers' effective mass m_{eff} by $\omega_{pl} = \sqrt{\frac{n_c e^2}{\varepsilon_\infty\epsilon_0 m_{\mathrm{eff}}}}$. The quantities γ_{pl} and γ_0 are the line width broadening of the plasmon peak and are determined by the plasmon relaxation time. For $\gamma_{pl} = \gamma_0$ in eq 13 one arrives at the well-known Drude term. For the Nb-STO we use $\omega_{pl} = 83$ meV, $\gamma_{pl} = 75$ meV, and $\gamma_0 = 5$ meV. The values are estimated by extrapolating the values measured by optical techniques at liquid nitrogen temperature to our measurement temperature ($T = 15$ K).[70,73] The extrapolation is based on the temperature dependence of effective mass as discussed in detail in ref 74. For FeSe ML we use a Drude term with $\omega_{pl} = 334$ meV estimated based on $\omega_{pl} = \sqrt{\frac{n_c e^2}{\varepsilon_\infty\epsilon_0 m_{\mathrm{eff}}}}$, assuming $m_{\mathrm{eff}} \simeq 3\ m_e$ and $n_c = 0.12\ e^-/\mathrm{Fe}$. The damping parameter was $\gamma_{pl} = \gamma_0 = 270$ meV.

The TO phonon frequencies and their damping as well as $|\mathcal{R}_{|\sigma\rangle}|^2$ serve as the input of the simulations. The values we used for our simulations are provided in Supporting Table 1S. The values of $|\mathcal{R}_{|\sigma\rangle}|^2$ depend on the incident energy. We take the values from Figure 2b based on the expression $\left|\mathcal{R}_{|+\rangle}\right|^2 = \frac{1 + A(E_i)}{2}$ and $\left|\mathcal{R}_{|-\rangle}\right|^2 = \frac{1 - A(E_i)}{2}$. For the data shown in Figure 4b the values are $|\mathcal{R}_{|+\rangle}|^2(E_i = 4\mathrm{eV}) = 0.555$ and $|\mathcal{R}_{|-\rangle}|^2(E_i = 4\mathrm{eV}) = 0.445$. For those shown in Figure 4d they are $|\mathcal{R}_{|+\rangle}|^2(E_i = 6\mathrm{eV}) = 0.53$ and $|\mathcal{R}_{|-\rangle}|^2(E_i = 6\mathrm{eV}) = 0.47$.

AUTHOR INFORMATION

Corresponding Author

Khalil Zakeri − *Heisenberg Spin-dynamics Group, Physikalisches Institut, Karlsruhe Institute of Technology, D-76131 Karlsruhe, Germany;* ◉ orcid.org/0000-0002-4674-3446; Phone: +49 (0)721 608 43861; Email: khalil.zakeri@kit.edu; Fax: +49 (0)721 608 46103

Authors

Dominik Rau − *Heisenberg Spin-dynamics Group, Physikalisches Institut, Karlsruhe Institute of Technology, D-76131 Karlsruhe, Germany*

Jasmin Jandke − *Physikalisches Institut, Karlsruhe Institute of Technology, D-76131 Karlsruhe, Germany*

Fang Yang − *Physikalisches Institut, Karlsruhe Institute of Technology, D-76131 Karlsruhe, Germany;* orcid.org/0000-0002-9152-1260

Wulf Wulfhekel − *Physikalisches Institut, Karlsruhe Institute of Technology, D-76131 Karlsruhe, Germany; Institute for Quantum Materials and Technologies, Karlsruhe Institute of Technology, D-76344 Eggenstein-Leopoldshafen, Germany*

Christophe Berthod − *Department of Quantum Matter Physics, University of Geneva, 1211 Geneva, Switzerland;* orcid.org/0000-0002-0787-008X

Author Contributions

Kh.Z. initiated the idea of the study, supervised the project, conceived and planned the experiments, analyzed the experimental data, performed the simulations, and wrote the paper. D.R. contributed to carrying out the SPHREELS experiments. F.Y., J.J., and W.W. prepared the samples and performed the STM experiments. C.B. carried out the theoretical modeling and derived all the analytical expressions for the spin-dependent scattering cross-sections.

Notes

The authors declare no competing financial interest.

REFERENCES

(1) Galitski, V.; Spielman, I. B. Spin-orbit coupling in quantum gases. *Nature* **2013**, *494*, 49−54.

(2) Winkler, R. *Spin-Orbit Coupling Effects in Two-Dimensional Electron and Hole Systems*, 1st ed.; Springer Tracts in Modern Physics; Springer: Berlin Heidelberg, 2003; Vol. *191*; pp 1−228.

(3) Moore, J. E. The birth of topological insulators. *Nature* **2010**, *464*, 194−198.

(4) Hasan, M. Z.; Kane, C. L. Colloquium: Topological insulators. *Rev. Mod. Phys.* **2010**, *82*, 3045−3067.

(5) Qi, X.-L.; Zhang, S.-C. Topological insulators and superconductors. *Rev. Mod. Phys.* **2011**, *83*, 1057−1110.

(6) Shen, S.-Q. *Topological Insulators*, 2nd ed.; Springer Series in Solid-State Sciences; Springer: Singapore, 2017; Vol. *187*; pp 1−266.

(7) He, K.; Wang, Y.; Xue, Q.-K. Topological materials: Quantum anomalous Hall system. *Annual Review of Condensed Matter Physics* **2018**, *9*, 329−344.

(8) Leijnse, M.; Flensberg, K. Introduction to topological superconductivity and Majorana fermions. *Semicond. Sci. Technol.* **2012**, *27*, 124003.

(9) Beenakker, C. Search for Majorana fermions in superconductors. *Annual Review of Condensed Matter Physics* **2013**, *4*, 113−136.

(10) Sato, M.; Ando, Y. Topological superconductors: a review. *Rep. Prog. Phys.* **2017**, *80*, 076501.

(11) Nayak, C.; Simon, S. H.; Stern, A.; Freedman, M.; Sarma, S. D. Non-Abelian anyons and topological quantum computation. *Rev. Mod. Phys.* **2008**, *80*, 1083−1159.

(12) Hao, N.; Hu, J. Topological quantum states of matter in iron-based superconductors: from concept to material realization. *National Science Review* **2019**, *6*, 213−226.

(13) Wang, Q.-Y.; et al. Interface-induced high-temperature superconductivity in single unit-cell FeSe films on SrTiO$_3$. *Chin. Phys. Lett.* **2012**, *29*, 037402.

(14) Liu, D.; et al. Electronic origin of high-temperature superconductivity in single-layer FeSe superconductor. *Nat. Commun.* **2012**, *3*, 931.

(15) Tan, S.; et al. Interface-induced superconductivity and strain-dependent spin density waves in FeSe/SrTiO$_3$ thin films. *Nat. Mater.* **2013**, *12*, 634−640.

(16) He, S.; et al. Phase diagram and electronic indication of high-temperature superconductivity at 65K in single-layer FeSe films. *Nat. Mater.* **2013**, *12*, 605−610.

(17) Bozovic, I.; Ahn, C. A new frontier for superconductivity. *Nat. Phys.* **2014**, *10*, 892−895.

(18) Ge, J.-F.; Liu, Z.-L.; Liu, C.; Gao, C.-L.; Qian, D.; Xue, Q.-K.; Liu, Y.; Jia, J.-F. Superconductivity above 100 K in single-layer FeSe films on doped SrTiO$_3$. *Nat. Mater.* **2015**, *14*, 285−289.

(19) Lee, J. J.; Schmitt, F. T.; Moore, R. G.; Johnston, S.; Cui, Y.-T.; Li, W.; Yi, M.; Liu, Z. K.; Hashimoto, M.; Zhang, Y.; Lu, D. H.; Devereaux, T. P.; Lee, D.-H.; Shen, Z.-X. Interfacial mode coupling as the origin of the enhancement of T$_c$ in FeSe films on SrTiO$_3$. *Nature* **2014**, *515*, 245−248.

(20) Kang, J.; Fernandes, R. M. Superconductivity in FeSe thin films driven by the interplay between nematic fluctuations and spin-orbit coupling. *Phys. Rev. Lett.* **2016**, *117*, 217003.

(21) Hao, N.; Shen, S.-Q. Topological superconducting states in monolayer FeSe/SrTiO$_3$(001). *Phys. Rev. B* **2015**, *92*, 165104.

(22) Borisenko, S. V.; Evtushinsky, D. V.; Liu, Z.-H.; Morozov, I.; Kappenberger, R.; Wurmehl, S.; Büchner, B.; Yaresko, A. N.; Kim, T. K.; Hoesch, M.; Wolf, T.; Zhigadlo, N. D. Direct observation of spin-orbit coupling in iron-based superconductors. *Nat. Phys.* **2016**, *12*, 311−317.

(23) Zakeri, K.; Engelhardt, T.; Wolf, T.; Tacon, M. L. Phonon dispersion relation of single-crystalline β−FeSe. *Phys. Rev. B* **2017**, *96*, 094531.

(24) Zakeri, K.; Engelhardt, T.; Tacon, M. L.; Wolf, T. Phonon spectrum of single-crystalline FeSe probed by high-resolution electron energy-loss spectroscopy. *Physica C: Superconductivity and its Applications* **2018**, *549*, 18−21.

(25) Zhang, S.; et al. Lattice dynamics of ultrathin FeSe films on SrTiO$_3$. *Phys. Rev. B* **2018**, *97*, 035408.

(26) Zhang, S.; Guan, J.; Jia, X.; Liu, B.; Wang, W.; Li, F.; Wang, L.; Ma, X.; Xue, Q.; Zhang, J.; Plummer, E. W.; Zhu, X.; Guo, J. Role of SrTiO$_3$ phonon penetrating into thin FeSe films in the enhancement of superconductivity. *Phys. Rev. B* **2016**, *94*, 081116.

(27) Jandke, J.; Yang, F.; Hlobil, P.; Engelhardt, T.; Rau, D.; Zakeri, K.; Gao, C.; Schmalian, J.; Wulfhekel, W. Unconventional pairing in single FeSe layers. *Phys. Rev. B* **2019**, *100*, 020503.

(28) Vig, S.; Kogar, A.; Mitrano, M.; Husain, A.; Venema, L.; Rak, M.; Mishra, V.; Johnson, P.; Gu, G.; Fradkin, E.; Norman, M.; Abbamonte, P. Measurement of the dynamic charge response of materials using low-energy, momentum-resolved electron energy-loss spectroscopy (M-EELS). *SciPost Physics* **2017**, *3*, 026.

(29) Husain, A. A.; Mitrano, M.; Rak, M. S.; Rubeck, S.; Uchoa, B.; March, K.; Dwyer, C.; Schneeloch, J.; Zhong, R.; Gu, G.; Abbamonte, P. Crossover of charge fluctuations across the strange metal phase diagram. *Physical Review X* **2019**, *9*, 041062.

(30) Zakeri, K.; Wettstein, J.; Sürgers, C. Generation of spin-polarized hot electrons at topological insulators surfaces by scattering

from collective charge excitations. *Communications Physics* **2021**, *4*, 225.

(31) Qin, H. J.; Zakeri, K.; Ernst, A.; Kirschner, J. Temperature dependence of magnetic excitations: Terahertz magnons above the Curie temperature. *Phys. Rev. Lett.* **2017**, *118*, 127203.

(32) Kirschner, J. *Polarized Electrons at Surfaces*, 1st ed.; Springer Tracts in Modern Physics; Springer: Berlin Heidelberg, 1985; Vol. *106*; pp 1−160.

(33) Zakeri, K.; Rau, D.; Wettstein, J.; Döttling, M.; Jandke, J.; Yang, F.; Wulfhekel, W.; Schmalian, J. Direct evidence of a charge depletion region at the interface of Van der Waals monolayers and dielectric oxides: The case of superconducting FeSe/STO. **2022**, 2210.02058, arXiv (Condensed Matter, Materials Science), DOI: 10.48550/arXiv.2210.02058 (accessed May 3, 2023).

(34) Mott, N. F.; Bohr, N. H. D. The scattering of fast electrons by atomic nuclei. *Proceedings of the Royal Society of London* **1929**, *124*, 425−442.

(35) Kessler, J. *Polarized Electrons*, 1st ed.; Springer Series on Atomic, Optical, and Plasma Physics; Springer: Berlin Heidelberg, 1985; Vol. *1*; pp 7−20.

(36) Feder, R. *Polarized Electrons in Surface Physics*, 1st ed.; World Scientific: Singapore, 1986; Vol. *1*; pp 1−632.

(37) Wang, G. C.; Dunlap, B. I.; Celotta, R. J.; Pierce, D. T. Symmetry in low-energy-polarized-electron diffraction. *Phys. Rev. Lett.* **1979**, *42*, 1349−1352.

(38) McRae, E. G. Electronic surface resonances of crystals. *Rev. Mod. Phys.* **1979**, *51*, 541−568.

(39) McRae, E. G.; Pierce, D. T.; Wang, G. C.; Celotta, R. J. Polarized-low-energy-electron-diffraction study of the mechanism of electron reflection from W(001) at low energies. *Phys. Rev. B* **1981**, *24*, 4230−4239.

(40) Sushkov, O. P.; Milstein, A. I.; Mori, M.; Maekawa, S. Relativistic effects in scattering of polarized electrons. *Europhys. Lett.* **2013**, *103*, 47003.

(41) Evans, E.; Mills, D. L. Theory of inelastic scattering of slow electrons by long-wavelength surface optical phonons. *Phys. Rev. B* **1972**, *5*, 4126−4139.

(42) Mills, D. The scattering of low energy electrons by electric field fluctuations near crystal surfaces. *Surf. Sci.* **1975**, *48*, 59−79.

(43) Ibach, H.; Mills, D. *Electron Energy Loss Spectroscopy and Surface Vibrations*, 1st ed.; Academic Press: New York, 1982; pp 105−120.

(44) Peng, R.; Zou, K.; Han, M. G.; Albright, S. D.; Hong, H.; Lau, C.; Xu, H. C.; Zhu, Y.; Walker, F. J.; Ahn, C. H. Picoscale structural insight into superconductivity of monolayer FeSe/SrTiO₃. *Science Advances* **2020**, *6*, eaay4517.

(45) Ma, M.; Bourges, P.; Sidis, Y.; Xu, Y.; Li, S.; Hu, B.; Li, J.; Wang, F.; Li, Y. Prominent role of spin-orbit coupling in FeSe revealed by inelastic neutron scattering. *Physical Review X* **2017**, *7*, 021025.

(46) Hao, N.; Hu, J. Topological Phases in the Single-Layer FeSe. *Physical Review X* **2014**, *4*, 031053.

(47) Wang, Z. F.; Zhang, H.; Liu, D.; Liu, C.; Tang, C.; Song, C.; Zhong, Y.; Peng, J.; Li, F.; Nie, C.; Wang, L.; Zhou, X. J.; Ma, X.; Xue, Q. K.; Liu, F. Topological edge states in a high-temperature superconductor FeSe/SrTiO₃(001) film. *Nat. Mater.* **2016**, *15*, 968−973.

(48) Liu, C.; Chen, C.; Liu, X.; Wang, Z.; Liu, Y.; Ye, S.; Wang, Z.; Hu, J.; Wang, J. Zero-energy bound states in the high-temperature superconductors at the two-dimensional limit. *Science Advances* **2020**, *6*, eaax7547.

(49) Wang, Y.; Linscheid, A.; Berlijn, T.; Johnston, S. *Ab initio* study of cross-interface electron-phonon couplings in FeSe thin films on SrTiO₃. *Phys. Rev. B* **2016**, *93*, 134513.

(50) Zhang, C.; et al. Ubiquitous strong electron−phonon coupling at the interface of FeSe/SrTiO₃. *Nat. Commun.* **2017**, *8*, 14468.

(51) Faeth, B. D.; Xie, S.; Yang, S.; Kawasaki, J. K.; Nelson, J. N.; Zhang, S.; Parzyck, C.; Mishra, P.; Li, C.; Jozwiak, C.; Bostwick, A.; Rotenberg, E.; Schlom, D. G.; Shen, K. M. Interfacial Electron-Phonon Coupling Constants Extracted from Intrinsic Replica Bands in Monolayer FeSe/SrTiO₃. *Phys. Rev. Lett.* **2021**, *127*, 016803.

(52) Rademaker, L.; Alvarez-Suchini, G.; Nakatsukasa, K.; Wang, Y.; Johnston, S. Enhanced superconductivity in FeSe/SrTiO₃ from the combination of forward scattering phonons and spin fluctuations. *Phys. Rev. B* **2021**, *103*, 144504.

(53) Liu, C.; et al. High-order replica bands in monolayer FeSe/SrTiO₃ revealed by polarization-dependent photoemission spectroscopy. *Nat. Commun.* **2021**, *12*, 4573.

(54) Graser, S.; Maier, T. A.; Hirschfeld, P. J.; Scalapino, D. J. Near-degeneracy of several pairing channels in multiorbital models for the Fe pnictides. *New J. Phys.* **2009**, *11*, 025016.

(55) Linscheid, A.; Maiti, S.; Wang, Y.; Johnston, S.; Hirschfeld, P. High T_C via Spin Fluctuations from Incipient Bands: Application to Monolayers and Intercalates of FeSe. *Phys. Rev. Lett.* **2016**, *117*, 077003.

(56) Liu, C.; Wang, Z.; Ye, S.; Chen, C.; Liu, Y.; Wang, Q.; Wang, Q.-H.; Wang, J. Detection of bosonic mode as a signature of magnetic excitation in one-unit-cell FeSe on SrTiO₃. *Nano Lett.* **2019**, *19*, 3464−3472.

(57) Song, Q.; Yu, T. L.; Lou, X.; Xie, B. P.; Xu, H. C.; Wen, C. H. P.; Yao, Q.; Zhang, S. Y.; Zhu, X. T.; Guo, J. D.; Peng, R.; Feng, D. L. Evidence of cooperative effect on the enhanced superconducting transition temperature at the FeSe/SrTiO₃ interface. *Nat. Commun.* **2019**, *10*, 758.

(58) Schrodi, F.; Aperis, A.; Oppeneer, P. M. Multichannel superconductivity of monolayer FeSe on SrTiO₃: Interplay of spin fluctuations and electron-phonon interaction. *Phys. Rev. B* **2020**, *102*, 180501.

(59) Bang, Y.; Stewart, G. R. Superconducting properties of the s-wave state: Fe-based superconductors. *J. Phys.: Condens. Matter* **2017**, *29*, 123003.

(60) Li, Z.; Peng, J.-P.; Zhang, H.-M.; Zhang, W.-H.; Ding, H.; Deng, P.; Chang, K.; Song, C.-L.; Ji, S.-H.; Wang, L.; He, K.; Chen, X.; Xue, Q.-K.; Ma, X.-C. Molecular beam epitaxy growth and post-growth annealing of FeSe films on SrTiO₃: a scanning tunneling microscopy study. *J. Phys.: Condens. Matter* **2014**, *26*, 265002.

(61) Zakeri, K. Elementary spin excitations in ultrathin itinerant magnets. *Phys. Rep.* **2014**, *545*, 47−93.

(62) Zakeri, K.; Kirschner, J. In *Probing magnons by spin-polarized electrons*, 1 st ed.; Demokritov, S. O., Slavin, A. N., Eds.; Topics in Applied Physics Magnonics From Fundamentals to Applications; Springer: Berlin, Heidelberg, 2013; Vol. *125*; Chapter 7, pp 84−99.

(63) Berthod, C. *Spectroscopic Probes of Quantum Matter*, 1st ed.; IOP Publishing: Bristol, 2018; pp 1−338.

(64) Zakeri, K.; Berthod, C. Theory of spin-polarized high-resolution electron energy loss spectroscopy from nonmagnetic surfaces with a large spin-orbit coupling. *Phys. Rev. B* **2022**, *106*, 235117.

(65) Šunjić, M.; Lucas, A. A. Multiple Plasmon Effects in the Energy-Loss Spectra of Electrons in Thin Films. *Phys. Rev. B* **1971**, *3*, 719−729.

(66) Lucas, A.; Šunjić, M. Fast-electron spectroscopy of collective excitations in solids. *Prog. Surf. Sci.* **1972**, *2*, 75−137.

(67) Lambin, P.; Vigneron, J.-P.; Lucas, A. Computation of the surface electron-energy-loss spectrum in specular geometry for an arbitrary plane-stratified medium. *Comput. Phys. Commun.* **1990**, *60*, 351−364.

(68) Lazzari, R.; Li, J.; Jupille, J. Dielectric study of the interplay between charge carriers and electron energy losses in reduced titanium dioxide. *Phys. Rev. B* **2018**, *98*, 075432.

(69) Yuan, R. H.; Dong, T.; Song, Y. J.; Zheng, P.; Chen, G. F.; Hu, J. P.; Li, J. Q.; Wang, N. L. Nanoscale phase separation of antiferromagnetic order and superconductivity in $K_{0.75}Fe_{1.75}Se_2$. *Sci. Rep.* **2012**, *2*, 221.

(70) Gervais, F.; Servoin, J.-L.; Baratoff, A.; Bednorz, J. G.; Binnig, G. Temperature dependence of plasmons in Nb-doped SrTiO₃. *Phys. Rev. B* **1993**, *47*, 8187−8194.

(71) Zhou, Y.; Millis, A. J. Dipolar phonons and electronic screening in monolayer FeSe on $SrTiO_3$. *Phys. Rev. B* **2017**, *96*, 054516.

(72) Zhou, Y.; Millis, A. J. Charge transfer and electron-phonon coupling in monolayer FeSe on Nb-doped $SrTiO_3$. *Phys. Rev. B* **2016**, *93*, 224506.

(73) Eagles, D. M.; Georgiev, M.; Petrova, P. C. Explanation for the temperature dependence of plasma frequencies in $SrTiO_3$ using mixed-polaron theory. *Phys. Rev. B* **1996**, *54*, 22−25.

(74) Collignon, C.; Bourges, P.; Fauqué, B.; Behnia, K. Heavy Nondegenerate Electrons in Doped Strontium Titanate. *Physical Review X* **2020**, *10*, 031025.